

layer material needed to insulate the ice below it from the solar radiation (13).

The idea that POM is an astrophysical material is not new. Wickramasinghe (14) suggested its existence to explain part of the interstellar extinction spectrum. Vanýsek and Wickramasinghe (15) suggested that POM can be responsible for certain observed features in the infrared spectrum of several comets. Mendis and Wickramasinghe (16) echoed these suggestions and considered additional properties of POM that strengthened the indirect evidence.

Polymer formation is one of the most characteristic properties of formaldehyde. It proceeds as an exothermic reaction. Mechanisms for polymerization at very low temperatures in interstellar space involve quantum tunneling of the activation potential (17). Cosmic radiation plays an important role in this process. However, several preliminary steps need to be investigated to complete the chemical sequence of formation, starting from the dominant constituents in interstellar clouds.

POM could have formed under the action of cosmic radiation on the surface layer of comet nuclei in the Oort cloud. However,

since POM is still being released from the comet, it appears that the dust that contains POM is also deep in the interior of the nucleus. The POM must have been created in interstellar space, the presolar nebula, or the solar nebula and was then incorporated into the cometsimals at the time of their formation. This would be consistent with the hypothesis that comets are the Rosetta stone of the solar nebula (18). However, POM is not as volatile as the icy component of a comet nucleus and its affinity for dust grains would make it even more stable. Frozen water is the least volatile and most abundant component of the ices in comet nuclei, and is also relatively stable. However, most of the other volatile icy components are present only at the level of a few percent. Their primordial abundance in cometsimals may have been quite different.

#### REFERENCES AND NOTES

1. A. Korth *et al.*, *Nature (London)* **321**, 335 (1986).
2. A. Korth *et al.*, *ESA SP-250* (European Space Agency, Paris, 1986), vol. 1, p. 199.
3. D. L. Mitchell *et al.*, *ibid.*, p. 203.
4. D. L. Mitchell, private communication.
5. W. F. Huebner *et al.*, in *Proceedings of the Symposium*

*on the Diversity and Similarity of Comets*, European Space Agency, Brussels, 6 to 9 April 1987 (European Space Agency, Paris, in press); D. L. Mitchell *et al.*, *Science* **237**, 626 (1987).

6. S. W. Shalaby, *Macromol. Rev.* **14**, 419 (1979).
7. A. Omont, in *Astrochemistry, International Astronomical Union Symposium No. 120*, M. S. Vardya and S. P. Tarafdar, Eds. (Reidel, Dordrecht, Netherlands, 1987), p. 545.
8. M. Combes *et al.*, *ESA SP-250* (European Space Agency, Paris, 1986), vol. 1, p. 353; L. E. Snyder, P. Palmer, I. de Pater, unpublished results.
9. P. Eberhardt *et al.*, *ESA SP-250* (European Space Agency, Paris, 1986), vol. 1, p. 383.
10. J. Kissel *et al.*, *Nature (London)* **321**, 280 (1986); J. Kissel *et al.*, *ibid.*, p. 336.
11. J. A. M. McDonnell *et al.*, *ibid.*, p. 338.
12. H. U. Keller *et al.*, *ibid.*, p. 320.
13. R. Z. Sagdeev *et al.*, *ibid.*, p. 259.
14. N. C. Wickramasinghe, *ibid.* **252**, 462 (1974); *Mon. Not. R. Astron. Soc.* **170**, 11P (1975).
15. V. Vanýsek and N. C. Wickramasinghe, *Astrophys. Space Sci.* **33**, L19 (1975).
16. D. A. Mendis and N. C. Wickramasinghe, *ibid.* **37**, L13 (1975).
17. V. I. Goldanskii, M. D. Frank-Kamenetskii, I. M. Barkalov, *Science* **182**, 1344 (1973); V. I. Goldanskii, *Sov. Phys. Dokl.* **22**, 417 (1977).
18. See R. A. Kerr, *Science* **234**, 1321 (1986).
19. Preprints from the PICCA instrument were made available by A. Korth, R. P. Lin, and D. L. Mitchell. Their willingness to share this information is acknowledged, as are the detailed and useful discussions with them and with D. A. Mendis. This work is supported by funds from the NASA Planetary Atmospheres program.

4 May 1987; accepted 7 July 1987

## High-Resolution Electron Microscopy and Scanning Tunneling Microscopy of Native Oxides on Silicon

A. H. CARIM, M. M. DOVEK, C. F. QUATE, R. SINCLAIR, C. VORST

High-resolution transmission electron microscopy and scanning tunneling microscopy have been combined to examine the structure of the thin "native" oxide that forms on silicon surfaces at room temperature. Differences in the cleaning procedures for silicon wafers may affect the morphology of this oxide and critically influence further processing on the silicon substrates. An etch that ended with a dip in hydrofluoric acid provided a thinner oxide and a lower interface step density than did a sulfuric peroxide treatment. The availability of complementary information from high-resolution transmission electron microscopy and scanning tunneling microscopy is discussed.

THE EXPOSURE OF SILICON TO AIR AT room temperature causes a thin layer of "native" oxide to form. The properties of this oxide affect subsequent epitaxy, metallization, oxidation, and electrical behavior and thus are critical in solid-state silicon technology. Chemical and optical characteristics of the native oxide on silicon have been investigated by methods such as x-ray photoelectron spectroscopy (XPS) (1, 2), electron energy loss spectroscopy (EELS) (2, 3), and ellipsometry (1, 4, 5). Such techniques have provided information on the oxide stoichiometry, density, impurities, and growth rates. Their disadvantages are that these techniques average signals from over a large area on the sample surface

and do not directly probe the nanometer-scale structure of the film.

Recently, two powerful tools have emerged for examining the structure of surfaces and interfaces. First, high-resolution transmission electron microscopy (HRTEM) has evolved into a well-characterized technique for profile imaging of interfaces (6) and surfaces (7). Second, scanning tunneling microscopy (STM) (8) provides a new method for obtaining a planar view of surface structure. In this report cross-sectional HRTEM and real-time STM imaging are combined to accurately determine native oxide thicknesses and examine silicon-oxide interface morphologies after two different cleaning procedures. Three major goals were achieved: (i) new information

on the structure of native oxide was obtained; (ii) the ability to gather complementary information from HRTEM and STM was realized; and (iii) STM imaging of a solid-state interface through a vacuum-dielectric bilayer barrier was demonstrated.

The wafers used in this experiment were *p*-type (100) slices with a resistivity  $\rho$  between 17 and 33  $\Omega$ -cm. Two cleaning treatments were examined. The "A" cleaning involved 10 minutes of immersion in a sulfuric peroxide solution (50 ml of  $H_2O_2$  added to an 8-liter  $H_2SO_4$  bath just prior to wafer cleaning) at 90° to 110°C followed by 10 seconds in 1:10 HF in deionized water (DI) mixed by volume. This procedure left a nearly bare silicon surface that formed a thin native oxide layer shortly after removal from the HF (1). The "B" cleaning involved 10 minutes of immersion in a 1:3:3 solution of  $HNO_3$ -HCl-DI followed by the 10 minutes of sulfuric peroxide treatment discussed above in A. This is similar to the so-called chemical oxide treatments (9), since it is thought that a small amount of oxide forms during the final cleaning step. Three hours

A. H. Carim and R. Sinclair, Department of Materials Science and Engineering, Stanford University, Stanford, CA 94305.

M. M. Dovek and C. F. Quate, E. L. Ginzton Laboratory, Stanford University, Stanford, CA 94305.

C. Vorst, Philips Research Laboratories Sunnyvale, Signetics Corporation, 811 East Arques Avenue, Sunnyvale, CA 94088.

of exposure to air allowed the stable native oxide layer to form. Samples for STM received no further processing. In order to better determine native oxide thickness and surface morphology for transmission electron microscopy, a polysilicon capping layer was added by chemical vapor deposition at 620°C. Cross-sectional HRTEM samples were prepared in the usual manner (10).

Electron microscopy was performed on the Philips EM430ST instrument, which allows resolution of the lattice points in silicon that are spaced 0.33 nm apart in the [01 $\bar{1}$ ] projection. Typical high-resolution micrographs from A and B samples are shown in Fig. 1. The wafer normal is the vertical [100] direction noted on the micrographs. Lattice points in the substrate, the mottled contrast of the amorphous oxide, and {111}-type lattice planes in the polysilicon overlayer are clearly visible. Note particularly that the imaging of lattice fringes in the polysilicon permits a clearer determination of the oxide layer thickness than was made by previous workers (11). The native oxide thickness for clean A ranged from 0.5 to 1.5 nm over fairly small lateral distances (<8 nm), as demonstrated in Fig. 1A. The average thickness was 1.0 nm. The oxide layer was continuous over all regions examined. Interfacial steps are occasionally larger than one atomic layer and on average are spaced 4.3 nm apart. Process B also resulted

in a continuous native oxide (Fig. 1B). In this case the thickness was somewhat greater (0.9 to 2.6 nm, with an average of 1.7 nm), as might be expected since some oxidation may occur in the sulfuric peroxide solution. The mean spacing of steps at the interface, however, decreased to about 2.6 nm. By approximating the sample thickness as 15 nm in the areas imaged and assuming no superposition effects, we calculated that the density of protrusions is on the order of  $0.8 \times 10^{12} \text{ cm}^{-2}$  for the A samples and  $1.3 \times 10^{12} \text{ cm}^{-2}$  for the B samples. Thus the treatment that ended with an oxidizing sulfuric peroxide bath led to about 50% more interfacial steps on the atomic scale.

We were able to perform real-time imaging in STM (12). Our microscope was operated in air initially and then in a low vacuum of 200 mtorr for improved tip stability at high bias. Tunneling through the oxide layer from the silicon surface prevented the observation of individual atoms, but the resolution was sufficient to identify small nonuniformities (on the scale of 1.0 nm) at the interface.

The assumption that no superposition occurs is unnecessary when we examine the interface morphology by STM, since a planar representation of the substrate-oxide interface is obtained from above. The wafer normal is thus perpendicular to the plane of the obtained images. Tunneling micro-

graphs for both samples taken with real-time current imaging are presented in Fig. 2. In this mode the tip is held at a constant distance from the sample. Differential changes in the tunneling current determine the contrast level in the image so that lighter shades correspond to higher local tunneling currents. The average tunneling current is maintained at a set value by a feedback loop.

For the A-cleaned sample, the STM was run in air with a bias on the tip  $V_b$  of +1.0 V and an average tunneling current  $I_t$  of 1.0 nA. Roughly circular features indicate silicon "bumps" at the interface, which were found to be approximately 1.5 nm in diameter, with an observed density of  $8 \times 10^{12}$  to  $10 \times 10^{12} \text{ cm}^{-2}$ . We illuminated the *p*-type semiconductor with visible white light in order to generate additional free electrons and thus enhance the tunneling process. This technique has previously proven useful in examining semi-insulating GaAs by STM (13).

The sample subjected to the B clean was more difficult to image because of the thicker oxide. Figure 2B was taken in a 200-mtorr environment with  $V_b = +5 \text{ V}$  and  $I_t = 1.3 \text{ nA}$ . A higher voltage was required primarily because the oxide was thicker. The features we saw were slightly smaller and somewhat more numerous. The observed density was  $15 \times 10^{12}$  to  $20 \times 10^{12} \text{ cm}^{-2}$  (that is, about twice that observed in the A-cleaned sample).

For comparison with the HRTEM results, we needed information about the interface from STM. Real-time STM images represent the modulation of barrier width as a function of position. Typically such images depict surfaces observed by electron tunneling through a single vacuum barrier. In this case, however, tunneling proceeds through an oxide-vacuum bilayer. The arguments below are made to demonstrate that the imaged current will depend much more strongly on the location of the Si-SiO<sub>2</sub> interface than on the relative position of the oxide-vacuum boundary.

Since macroscopic features are being imaged, a band representation appropriately describes the tunneling process. Figure 3 depicts the band structure of the metal-vacuum-oxide-semiconductor system for a *p*-type sample and a positive bias on the tip ( $+V_b$ ). To maintain a stable current without driving the tip into the insulator, it was desirable to maximize the tunneling current. This requires a positive value of  $V_b$  and a large number of electrons in the silicon conduction band, which was accomplished in the present study by optically generating additional electrons in *p*-type samples. The barrier  $V(x)$  between the boundaries  $x_1$  and  $x_2$  is shown in Fig. 3 with a dashed line. The

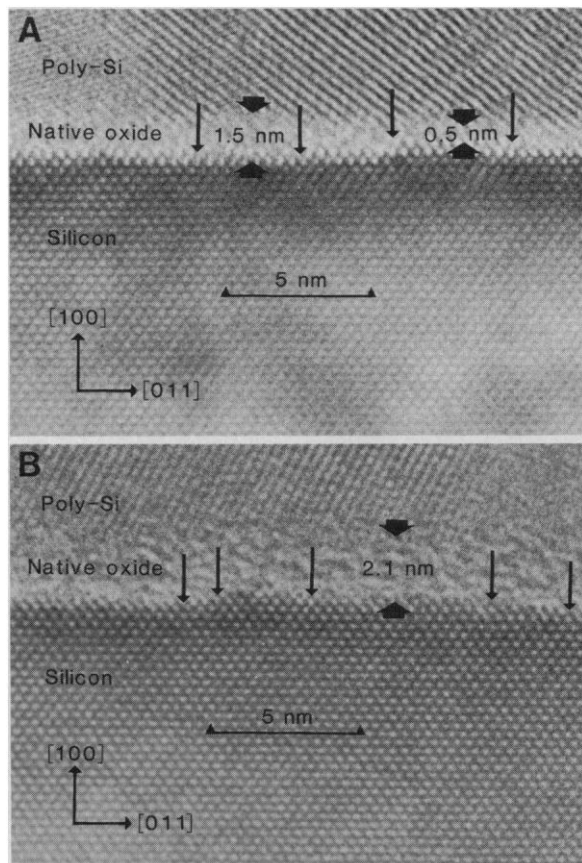


**Fig. 1.** Cross-sectional high-resolution micrographs of Si(100) samples that underwent cleaning treatments that ended with (A) an HF treatment (A cleaning) or (B) a sulfuric peroxide step (B cleaning). Arrows indicate interfacial steps and oxide thickness variations in (A). The density of stepped areas in these micrographs may vary somewhat from the average values for each sample.

current  $J$  through this barrier is (14)

$$J = \frac{q}{2\pi h} \iint T_t [F_1(E) - F_2(E)] dk_T^2 dE \quad (1)$$

where  $q$  is the electron charge,  $h$  is Planck's constant,  $T_t$  is the tunneling probability,  $E$  is the electron energy,  $F_1(E)$  and  $F_2(E)$  are the Fermi distribution functions in the tip and sample, respectively, and  $k_T$  is the transverse momentum. The Wentzel-Kramers-Brillouin approximation gives a relation between  $T_t$  and the barrier height  $[V(x) - E]$

$$T_t = \exp \int_{x_1}^{x_2} \left\{ \frac{8\pi^2 m^*}{h^2} [V(x) - E] \right\}^{1/2} dx \quad (2)$$

where  $m^*$  is the effective mass of the carrier.

Examination of Eq. 2 indicates that small variations in the substrate-native oxide interface location ( $\delta_{s-o}$ ) change the tunneling probability by approximately  $\exp[-A(\delta_{s-o})$

$(3.25 \text{ eV})^{1/2}]$ , where  $A$  is a constant. Such variations at the oxide-vacuum interface ( $\delta_{o-v}$ ) alter  $T_t$  by approximately  $\exp\{-A(\delta_{o-v}) [(4.15 \text{ eV})^{1/2} - (3.25 \text{ eV})^{1/2}]\}$ . The latter effect is significantly smaller for comparable values of  $\delta_{o-v}$  and  $\delta_{s-o}$ , as shown schematically in Fig. 4. Since the HRTEM images demonstrate that variations in the oxide surface are less than or similar in magnitude to those at the substrate-oxide interface, tunneling is dominated by the morphology of the silicon-native oxide boundary. Changes in oxide thickness are simple combinations of the changes in interface locations, and again  $\delta_{s-o}$  will dominate.

The density of features observed by HRTEM is about one-tenth of those seen in the STM images. The presence of a second interface is not responsible, as shown above. The features scaled appropriately with changes in the area scanned in STM, which confirmed that these are real variations in the sample and not artifacts due to instru-

mental noise, tip morphology, or capacitive coupling between the signals that controlled the piezoelectric scanning drives and the tunneling current. Since single-monolayer steps are detectable in the HRTEM micrographs, the additional features imaged by STM cannot be due to smaller steps.

The most probable cause of the discrepancy is the effect of projection in HRTEM (6). The superposition of several individual protrusions may result in only one apparent atomic ledge. Also, irregularities with very small lateral dimensions may not provide sufficient image contrast when masked by amorphous oxide in the direction of the electron beam. These phenomena may be visualized by projecting the STM images of Fig. 2 onto either of the lateral axes. Additionally, STM provides information about the shape of the stepped areas. Rather than having ledges that extend for long distances across the sample, as have been seen with reflection electron microscopy for clean on-axis Si(111) surfaces (15) and vicinal surfaces of metals (16), STM shows that on-axis Si(100) samples with a native oxide display steps that extend over small, roughly circular, and occasionally overlapping regions. Thus the STM data provide a better representation of the true feature densities and shapes.

In this study transmission electron microscopy was required in order to find the interfacial defects and identify their nature. The wide range of magnifications available in the transmission electron microscope established the scale and depth distribution of features of interest. HRTEM readily differentiated between pinholes or inclusions in the dielectric, interfacial precipitates, and steps or protrusions at the interface. Such effects might not have been readily distinguished by STM. However, STM provided a more detailed view of the interfacial plane and was invaluable for clarifying the shape and distribution of nanometer-scale features. The coupling of these techniques offers great promise for atomic-level characterization of materials.

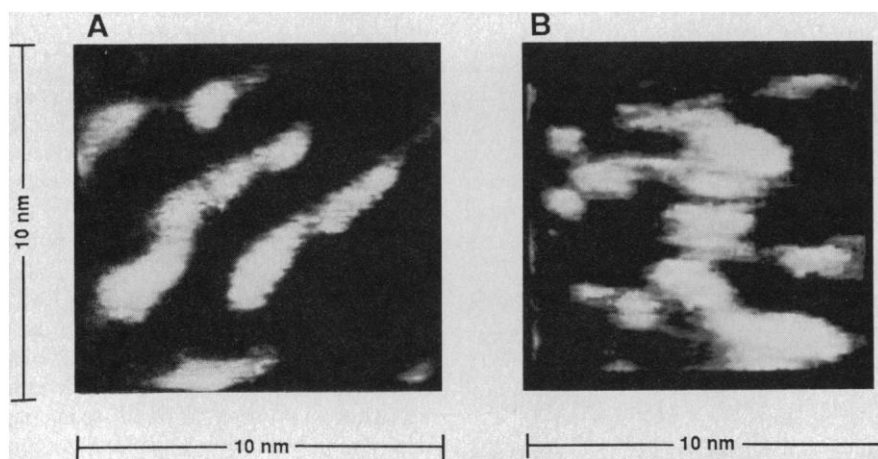


Fig. 2. Real-time STM images of native oxide samples after (A) the A cleaning and (B) the B cleaning. The [100] wafer normal is perpendicular to the plane of the images, toward the reader.

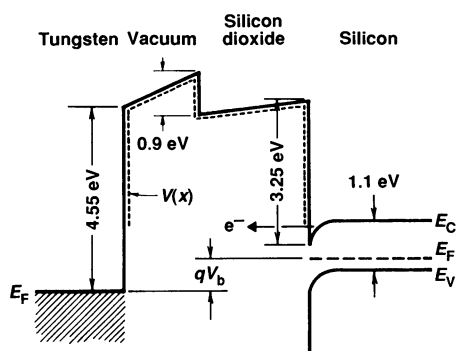


Fig. 3. Schematic band structure of the tungsten/vacuum/oxide/p-type semiconductor system for positive  $V_b$ . The energies  $E_F$ ,  $E_C$ , and  $E_V$  are the energies of the Fermi level, the conduction band edge, and the valence band edge, respectively. The energy  $qV_b$  is the electron charge times the applied bias and represents the difference in electric potential between the tunneling tip and the sample.

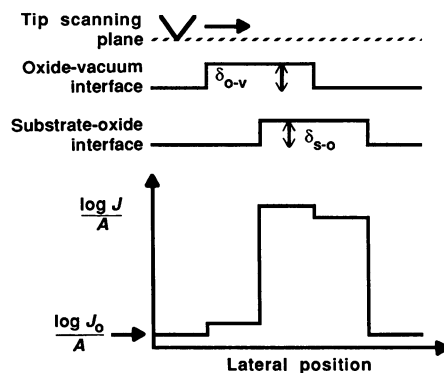


Fig. 4. Diagram that illustrates the spatial variation in the logarithm of the current density as a result of equally sized steps at the substrate-oxide and oxide-vacuum interfaces. The plot is to scale.

#### REFERENCES AND NOTES

1. S. I. Raider, R. Flitsch, M. J. Palmer, *J. Electrochem. Soc.* **122**, 413 (1975).
2. M. Grundner and H. Jacob, *Appl. Phys. A* **39**, 73 (1986).
3. H. Ibach, H. D. Bruchmann, H. Wagner, *ibid.* **29**, 113 (1982).
4. R. J. Archer, *J. Electrochem. Soc.* **104**, 619 (1957).
5. F. Lukes, *Surf. Sci.* **30**, 91 (1972).
6. A. H. Carim and R. Sinclair, *Mater. Lett.* **5**, 94 (1987).
7. D. J. Smith, *Surf. Sci.* **178**, 462 (1986).
8. G. Binnig, H. Rohrer, Ch. Gerber, E. Weibel, *Phys. Rev. Lett.* **49**, 57 (1982).
9. J. C. Bravman, G. L. Patton, J. D. Plummer, *J. Appl. Phys.* **57**, 2279 (1985).
10. J. C. Bravman and R. Sinclair, *J. Electron Microsc. Tech.* **1**, 53 (1984).

11. J. H. Mazur, R. Gronsky, J. Washburn, *Inst. Phys. Conf. Ser. No. 67* (1983), p. 77.
12. A. Bryant, D. P. E. Smith, C. F. Quate, *Appl. Phys. Lett.* **48**, 832 (1986).
13. G. F. A. van de Walle, H. van Kempen, P. Wyder, P. Davidsson, *ibid.* **50**, 22 (1987).
14. S. M. Sze, *Physics of Semiconductor Devices* (Wiley, New York, 1981), pp. 513-565.
15. N. Osakabe, Y. Tanishiro, K. Yagi, G. Honjo, *Surf. Sci.* **109**, 353 (1981).
16. T. Hsu, *Ultramicroscopy* **11**, 167 (1983).
17. We thank D. P. E. Smith, M. Richter, and J.

Nogami for their experimental assistance and invaluable comments. A.H.C. acknowledges support and guidance from Philips Research Laboratories Sunnyvale, Signetics Corporation, and in particular helpful discussions with W. T. Stacy. The HRTEM was purchased with funds from Stanford University, the Pew Foundation, and the NSF-MRL program of the National Science Foundation. The STM portion of this work was supported by the Defense Advanced Research Projects Agency.

6 April 1987; accepted 17 June 1987

## Radioactive Cesium from the Chernobyl Accident in the Greenland Ice Sheet

C. I. DAVIDSON, J. R. HARRINGTON, M. J. STEPHENSON,  
M. C. MONAGHAN, J. PUDYKIEWICZ, W. R. SCHELL

**Measurements of cesium-134 and cesium-137 in Greenland snow together with models of long-range transport have been used to assess radionuclide deposition in the Arctic after the Chernobyl accident. The results suggest that a well-defined layer of radioactive cesium is now present in polar glaciers, providing a new reference for estimating snow accumulation rates and dating ice core samples.**

NUCLEAR WEAPONS TESTS IN THE 1950s, 1960s, and 1970s emitted large amounts of man-made radioisotopes into the atmosphere. Some of this material eventually reached glaciers in the Arctic and Antarctic regions, providing a permanent record of the deposition of radioactivity associated with specific tests. These radioactive signatures have been used to determine snow accumulation rates, to date ice core samples analyzed for other contaminants, and to study long-range atmospheric transport (1). Emissions from the explosion and fire at the Chernobyl nuclear reactor in April 1986 have resulted in an additional radioactive layer in polar glaciers. This layer is of considerable interest: unlike weapons tests, which injected radioactive material into the stratosphere where residence times are more than a year, the Chernobyl emissions were confined to the troposphere where residence times are at most a few weeks (2). The resulting deposition thus occurred over a relatively short period, and this enables us to assign a narrow time interval to the radioactive layer. In the present study, we identify the Chernobyl signature in the Greenland Ice Sheet. We also attempt to relate characteristics of the deposited radioactivity to the atmospheric transport pathways and deposition processes involved.

Samples were collected from a snowpit 23 km southwest of Dye 3, Greenland, in late July 1986. This location is near the ice coring site established by Mayewski *et al.* (3). The snowpit walls were sampled in

continuous adjacent layers to a depth of 1.5 m under strict contamination control (3-5). The density was measured in each 5-cm layer, and the presence of ice strata and other distinguishing characteristics was recorded. Samples were collected each 5 cm for  $\delta^{18}\text{O}$  analysis (6), and each 10 cm for radioactive cesium analysis (7).

Results of these analyses show that detectable levels of  $^{134}\text{Cs}$  and  $^{137}\text{Cs}$  occurred only in one layer, between 10 and 20 cm below the surface. The concentrations in three identical samples extracted from this layer are  $2.0 \pm 0.8$  pCi/liter for  $^{134}\text{Cs}$  and  $6.2 \pm 1.4$  pCi/liter for  $^{137}\text{Cs}$  (average  $\pm$  standard deviation). If we take into account the thickness of the layer and the density of the snow, these values correspond to total (wet plus dry) deposits of  $0.072 \pm 0.030$  mCi/km<sup>2</sup> for  $^{134}\text{Cs}$  and  $0.22 \pm 0.05$  mCi/km<sup>2</sup> for  $^{137}\text{Cs}$ . All of the data have been corrected to 1 May.

These deposition rates are much smaller than corresponding values measured in Europe shortly after the accident. For example, deposition onto soil and vegetation was highly variable throughout Scandinavia, Germany, the United Kingdom, and the Mediterranean region, with values for both radionuclides ranging from <1 to several thousand millicuries per square kilometer (2, 8). Deposition rates to bulk wet-dry collectors in North America were closer to, but still somewhat greater than, the Dye 3 snow values. Seven sites in the Canadian Arctic had total deposition rates averaging 0.3 mCi/km<sup>2</sup> for  $^{134}\text{Cs}$  and 0.7 mCi/km<sup>2</sup> for

$^{137}\text{Cs}$  during May (9). Total deposition rates of  $^{134}\text{Cs}$  at sites in the western United States were typically 1 to 2 mCi/km<sup>2</sup>, with Midwest and East Coast locations reporting 0.1 to 1 mCi/km<sup>2</sup> (10, 11). Values for  $^{137}\text{Cs}$  in the United States were generally two to three times as large as those for  $^{134}\text{Cs}$ , consistent with the  $^{137}\text{Cs}/^{134}\text{Cs}$  activity ratio of  $3.0 \pm 0.24$  observed in Greenland. A single sample of the 10- to 20-cm layer was also analyzed for  $^{90}\text{Sr}$ , giving  $^{137}\text{Cs}/^{90}\text{Sr}$  equal to 20.2 corrected to 1 May (12). In comparison, values of this ratio in accumulated deposition on soil and vegetation were 19.0 in Denmark (13) and 24.4 in Italy (14).

Figure 1 shows the calculated dispersion of  $^{137}\text{Cs}$  from Chernobyl during late April and early May, based on an Eulerian long-range transport model. The simulation was developed by Pudykiewicz specifically for assessing atmospheric transport of emissions from the accident (15). This figure indicates that a portion of the radioactive cloud crossed Greenland near the end of April. The cloud continued moving south and west, reaching Canada and eventually the United States in early May. This scenario is consistent with available data: airborne measurements show that  $^{134}\text{Cs}$  and  $^{137}\text{Cs}$  from Chernobyl first reached the community of Alert in the northeastern Canadian Arctic on 1 May, the area north of Hudson Bay on 2 May, and sites in Alaska, southern Canada, and continental United States sometime between 6 and 10 May (9, 11). Furthermore, comparisons between results of the model and measured ground-level concentrations at several locations in Canada show good quantitative agreement (15). The dispersion patterns in Fig. 1 are similar to those calculated by Lawrence Livermore National Laboratory with a different simulation technique (16).

How did this atmospheric material reach the surface of the Greenland Ice Sheet? To explore this question, the  $\delta^{18}\text{O}$  data from the snowpit have been compared with the meteorological records from Dye 3 to identify the most probable time period and the specific storms represented by the 10- to 20-cm layer. The method has been discussed elsewhere (5). The procedure indicated that this layer corresponds to a time interval containing the following storms (with accumulation rates in centimeters of snow): 9

C. I. Davidson, J. R. Harrington, M. J. Stephenson, Departments of Civil Engineering and Engineering and Public Policy, Carnegie Mellon University, Pittsburgh, PA 15213.

M. C. Monaghan, Department of the Geophysical Sciences, University of Chicago, Chicago, IL 60637.

J. Pudykiewicz, Environment Canada, 2121 Trans-Canada Highway, Dorval, QU H9P 1J3 Canada.

W. R. Schell, Graduate School of Public Health, University of Pittsburgh, Pittsburgh, PA 15261.